Nanofibers of chitosan-polycaprolactone blends as active support for photocatalytic nanoparticles: Outstanding role of chitosan in the degradation of an organic dye in water

Nanofibers of chitosan-polycaprolactone blends as active support for photocatalytic nanoparticles: Outstanding role of chitosan in the degradation of an organic dye in water

Alexander Cordoba [a,b], Moreno Guernelli [b], Marco Montalti [b], Cesar Saldías [a], Maria Letizia Focarete [b,c], Angel Leiva [a,*]

[a] Department of Physical Chemistry, Faculty of Chemistry and Pharmacy, Pontificia Universidad Católica de Chile, Santiago, Chile
[b] Department of Chemistry "Giacomo Ciamician" and National Consortium of Materials Science and Technology (INSTM, Bologna RU), Alma Mater Studiorum - Università di Bologna, Bologna, Italy
[c] Health Sciences and Technologies-Interdepartmental Center for Industrial Research, Alma Mater Studiorum - Università di Bologna, Bologna, Italy

ARTICLE INFO

Keywords:
Nano composites
Hybrid composites
Electro-spinning
Nano particles
Synergism
Polymer fibers

ABSTRACT

Hybrid nanofibers of a chitosan-polycaprolactone blend containing titanium dioxide nanoparticles TiO_2NPs, were prepared through electrospinning to study their adsorption and photocatalytic degradation capabilities of the model organic water pollutants, rhodamine B, RhB. To obtain uniform and bead-free nanofibers, an optimization of the electrospinning parameters was performed. The optimization was carried out by systematically adjusting the solution conditions (solvent, concentration, and polymer ratio) and instrumental parameters (voltage, needle tip-collector distance, and flow). The obtained materials were characterized by FT-IR, TGA, DSC, SEM, TEM, mechanical tensile test, and water contact angle. The photoactivity was investigated using a batch-type system by following UV–Vis absorbance and fluorescence of RhB.

TiO_2NPs were incorporated ex-situ into the polymer matrix, contributing to good mechanical properties and higher hydrophilicity of the material. The results showed that the presence of chitosan in the nanofibers significantly increased the adsorption of RhB and its photocatalytic degradation by TiO_2NPs (5, 55 and 80 % of RhB degradation with NFs of PCL, TiO_2/PCL and TiO_2/CS-PCL, after 30 h of light irradiation, respectively), evidencing a synergistic effect between them. The results are attributed to an attraction of RhB by chitosan to the vicinity of TiO_2NPs, favouring initial adsorption and degradation, phenomenon known as "bait-and-hook-and-destruct" effect.

1. Introduction

Clean water availability is one of the most dramatic problems for current and future generations [1]. The current population growth, environmental pollution, and negative aspects of climate change strongly influence the availability of water suitable for human consumption worldwide. Indeed, future projections indicate that 57 % of the world's population will experience water shortages by 2050 [1]. The above is further aggravated considering that diverse organic and inorganic pollutants, such as pesticides, pharmaceuticals, dyes and heavy metals, have been detected in a significant number of water sources (lagoons, drinking water reservoirs, river channels) [2]. Therefore, the search for solutions that allow an efficient and environmentally friendly approach to this problem is very necessary nowadays.

Advanced oxidation processes (AOP) emerge as an innovative green chemical strategy to degrade the main organic pollutants present in wastewater [2,3]. The most frequently applied AOP methods are: i) Fenton-based processes, ii) heterogeneous photocatalysis, and iii) ozonation [2]. The heterogeneous photocatalysis, based on the use of semiconductor materials and light is especially interesting. Semiconductors are characterized by having a band gap energy (Eg), which is referred to as the energy difference between the top of the valence band to the bottom of the conduction band. The use of this type of photoactive material emerges as a promising strategy in the degradation of organic pollutants induced by light in the UV–visible range. It is well documented that by irradiating semiconductors with the appropriate energy

($h\nu \geq Eg$), excitons are generated that can evolve in the formation of electrons and holes on the surface of the material. This can lead to redox reactions that promote the in situ formation of reactive oxygen species (ROS) such as hydroxyl radicals, superoxide anion, or singlet oxygen [2,4–6]. Short-lived reactive species that can degrade not only organic pollutants but also viruses and bacteria [7–9].

In the 1970s, the pioneering works of Fukushima and co-workers [10], and Frank and Bard [11] demonstrated the photocatalytic properties exhibited by titanium dioxide (TiO_2) in heterogeneous media. This material is considered a reference due to its special attributes, such as, photochemical stability, low cost, bandgap energy in the UV range, and its remarkable photoactivity [2,4,5]. Recently, many efforts have been carried out to enhance TiO_2 photoactivity and solve some inherent limitations (e.g., fast charge recombination and low visible light activity) [12]. Since photocatalytic performances depend extensively on surface properties, one of the most exploited strategies consists of TiO_2 colloidal nanosystem synthesis [13]. This contributes to a significantly increased surface/volume ratio. However, nanoparticles (NPs) tend to agglomerate spontaneously, reducing the effective surface area and decreasing the photocatalytic activity over time. Additionally, the recovery of NPs from the reaction medium for efficient further reuse is also a challenging task to date [13]. To overcome these drawbacks, numerous studies have been carried out to support photocatalytic nanoparticles on different materials. Polymeric materials, glass and inorganic fabrics are among the most commonly used supports [14].

Electrospun polymer nanofibers have emerged as promising alternative to act as a versatile, stable and potentially active platform for application in heterogeneous catalysis. Nanofibers (NFs) display unique functional properties, such as submicrometric diameter, large specific surface area, and high aspect ratio. These materials can be obtained as macroscopic porous non-woven structures characterized by flexibility and elasticity. Importantly, this type of polymer matrix with a considerable amount of pores and chemical functionality can play a key role in stabilizing and enhancing the photoactivity of semiconductor and metal nanoparticles. Hybrid materials based on different types of polymeric NFs and photoactive NPs, have been reported in the literature, with potential applications in the light-driven removal of organic pollutants from water. Most of the studies carried out to date exploited synthetic polymers, and only in a few cases natural polymers, biopolymers, or biodegradable polymers have been considered [15]. PAN and PVDF electrospun fibers have been mostly used in recent years mainly due to its excellent thermal, mechanical stability and high chemical resistance [16–23]. The use of other polymers such as PMMA, PCL and CAB has also been reported [24,25].

Chitosan (CS) is one of the most promising natural polymers due to its recognized properties, biocompatibility, biodegradability, non-toxicity, and antimicrobial activity. Chitosan is a natural polysaccharide derived from chitin, which possesses numerous polar and ionizable groups and therefore has a high affinity for water [26,27]. However, CS has inherently poor processability by electrospinning and it is necessary to blend it with synthetic polymers to obtain electrospun nanofibers assemblies [28,29]. In this regard, an ideal candidate with excellent attributes, such as biocompatibility, biodegradability, non-toxicity, and good mechanical properties, is poly(caprolactone) (PCL). Particularly, this aliphatic polyester can be used to form polymer blends displaying high miscibility and compatibility whit chitosan, and improving its processability [26,30].

There are reports on the use of PCL nanofibers containing TiO_2 nanoparticles in different applications. Karagoz et al. conducted a study on PCL/TiO_2 NFs for photocatalysis. Their research focused on testing the degradation of methylene blue and ibuprofen under UV irradiation, achieving approximately a 60 % degradation rate. Furthermore, the authors reported that the introduction of Ag into the NFs enhanced degradation and conferred antibacterial properties [31]. Peng et al. produced porous fibers composed of PCL/TiO_2/Rectorite, displaying excellent degradation properties for organic dyes. The well-dispersed TiO_2 nanoparticles on the fibers surface facilitated their application in wastewater pollutant removal. In this context, PCL/TiO_2 demonstrated an 80 % degradation of rhodamine B within a 300-minute timeframe [32].

On the other hand, Karthega et al. employed electrospinning to create PCL/TiO_2 nanofibers over AM50 as a collector for biomedical purposes. Their investigation observes the formation of hydroxyapatite and revealed a significant improvement in cell adhesion and growth, likely attributed to the biocompatible nature of TiO_2 NPs [33]. Ahmadi et al. blended PCL with a natural polymer as gelatin, and TiO_2 NPs. They developed functional biomimetic scaffolds aimed at enhancing the osteoblastic differentiation of human adipose-derived stem cells while incorporating metformin [34].

Besides, some studies have explored the application of PCL/CS NFs in conjunction with NPs. For instance, Hadjianfar et al. suscesfully produced PCL/Chitosan-Fe_3O_4 core shell NFs, presenting a multifaceted approach to anticancer drug delivery [35]. Meanwhile, Amini et al., developed a nanomaterial composed by NFs of a PCL-CS copolymer and magnetic bioactive glasses for bone cancer treatment, which facilitates the controlled release of cisplatin [36]. These studies illustrate the versatility of PCL, CS and TiO_2 as components of different nanomaterials in various applications, ranging from photocatalysis to biomedical applications. However, the use of CS/PCL NFs containing TiO_2 NPs for the photocatalytic degradation of water pollutants, to the best of our knowledge has not been addressed.

To date, only one study in the biomedical area, using the electrospun CS/PCL/TiO_2 nanocomposite for in vivo wound healing, has been available, which showed improved wound healing compared to the CS/PCL preparation alone [37].

Herein, the fabrication of hybrid nanofibers from a CS-PCL blend containing TiO_2 NPs (TiO_2/CS-PCL) for adsorption and photocatalytic degradation of a model organic pollutant is presented for the first time. The excellent adsorption properties of CS and the good mechanical properties of PCL were combined to produce polymer nanofibers with improved properties. TiO_2 semiconductor nanoparticles were embedded in the NFs, which along with CS, produced a synergistic effect in the degradation of Rhodamine B under UV–vis light.

2. Materials and methods

2.1. Materials

Chitosan (Medium molecular weight) and PCL ($\overline{M}_n$80,000 g mol^{-1}) were supplied by Sigma Aldrich. Titanium oxide nanopowder (Sigma Aldrich, ≥99.5 %), Formic acid (Sigma Aldrich, 98 %), acetic acid (Sigma Aldrich, 99.8 %), hydrochloric acid (HCl, Sigma Aldrich, 37 %), Rhodamine B (RhB, Merck) were used. All reagents, solvents and chemicals were used without further purification unless otherwise stated. Ultrapure water was produced with a Millipore system (higher than 18.2 MΩcm resistivity).

2.2. Nanofibers preparation

Different polymer concentrations in a mixed acetic acid: formic acid solvent (1:1 v) were tested in order to obtain homogeneous and bead-free NFs.

Optimal working conditions were obtained with a 6 wt% PCL concentration and using a CS:PCL ratio of 10:90. A 5 wt% (with respect of total mat weight) of commercial TiO_2NPs was used to obtain reproducible electrospun samples.

In the general procedure, dry TiO_2 NPs were ultrasonicated in a mixed acetic acid: formic acid solvent (1:1 v/v) for 30 min. Subsequently, the appropriate amount of CS and PCL was added to the prepared dispersion and left under stirring for two more hours. The dispersion was then used for the electrospinning process.

A single needle apparatus (Spinbow Lab Unit, Spinbow s.r.l. Italy) was used for electrospinning. The polymer solution was supplied at a flow rate of 0.6 mL/h, through a PTFE tube and a 24 G needle. A grounded aluminium plate positioned 12.5 cm from the needle tip acted as a collector. Electrospinning was carried out at room temperature (22 ± 5 °C) and relative humidity of 35 ± 5 %.

2.3. Characterization of electrospun NFs

The morphology of the electrospun NFs was examined in a Leica / Cambridge Stereoscan 360 scanning electron microscope (SEM). Before SEM measurements, samples were coated with gold using a sputtering coater. Fibers diameter distribution was determined by measuring about 400 fibers of SEM images using Image-J software. The morphology of TiO_2NPs on polymeric NFs was observed by transmission electron microscopy (TEM) using a Philips microscope with an accelerating voltage of 80 kV. For this purpose, the NFs were electrospun directly on a 100 mesh TEM copper grid.

Differential Scanning Calorimetry (DSC) measurements were carried out using a TA instruments Q100 DSC equipped with a Liquid Nitrogen Cooling System (LNCS) accessory. Scans were performed from 90 to 150 °C in a nitrogen atmosphere at 20 °C/min. Two cooling cycles were performed: (1) controlled cooling at 10 °C/min and (2) a quench cooling.

The crystallinity degree (χ%) of PCL in the NFs was calculated using the following equation:

$$\chi_c \left(\frac{\Delta H_m}{\Delta H_m^0 x\left(\frac{\%w_{PCL}}{100}\right)} \right) x100 \quad (1)$$

Where ΔH_m is the melting enthalpy of PCL in the NFs, ΔH_m^0 is the theoretical melting enthalpy of 100 % crystalline PCL, which was considered as 142.0 Jg^{-1} [38], and $\%w_{PCL}$ is the weight percent PCL in the sample (obtained from thermogravimetric analyses).

Thermogravimetric analyses (TGA) were carried out using a TGA Q500 analyser (TA instruments) from room temperature to 600 °C at 10 °C/min under nitrogen atmosphere. The multi-material composition of the hybrid systems was determined by comparing the residual weights at 600 °C of each sample using the following equations:

$$\sum_i Rt(\%)_i^0 \bullet Wf_i^{Blend} \quad Rt(\%)_{Blend} \quad (2)$$

$$\sum_i Wf_i^{Blend} \quad 1 \quad (3)$$

Where $Rt(\%)_i^0$ represents the residual weight percentage of the i-th component, Wf_i^{Blend} is the weight fraction of the i-th component in the blend, and Rt (%) blend is the residual weight percentage of the electrospun mat with all components.

The chemical nature of the materials was analysed by Fourier Transform Infrared spectrometry (FT-IR) using a Spectrum Two instrument with an Attenuated Total Reflectance (ATR) accessory (Perkin-Elmer). FTIR spectra were recorded in the 4000–400 cm^{-1} range with a resolution of 4 cm^{-1}, accumulation of 16 scans and a step increment of 1 cm^{-1}.

The mechanical properties were determined using a TA Instrument DMA Q800 on rectangular sheets cut from the electrospun mats. The samples were cut 5 mm wide and 50 mm long. The thickness of each sample was measured using a digital micrometer. Measurements were carried out in tension mode at a single strain rate of 5 mm/min at room temperature. Load-displacement curves were obtained and converted to stress-strain curves. At least five replicates were run for each specimen, and the results were reported as an average value with its corresponding standard deviation.

Static contact angle measurements were performed using KSV's CAM 100 under ambient conditions. Lateral profiles of deionized water droplets were recorded for subsequent image analysis. Five droplets were observed in different areas of each electrospun mat and the results were reported as an average value with its corresponding standard deviation.

2.4. Evaluation of Rhodamine B adsorption

The RhB adsorption capacity of the electrospun materials was determined in batch-type systems. For this purpose, 2 cm^2 mat (~2 mg) was immersed in 20 mL of a dye solution at 1 mg/L under constant agitation. The whole experiment was performed in total darkness, and the concentration of the contaminant over time was monitored by UV–Visible spectroscopy using an Agilent Cary 60 spectrophotometer. The NFs of PCL, CS-PCL, TiO_2NPs/CS-PCL and TiO_2NPs/PCL were confronted with observing their effect on the adsorption of the contaminants.

2.5. Photodegradation kinetics

To study the photocatalytic activity of the electrospun mats, rhodamine B (RhB) was used as a model pollutant. The activity was evaluated by means of two methods: the first consisted of continuing with the same batch system as in Section 2.4 and initiating the photocatalytic reactions by irradiation with LEDs of white light (see emission spectrum in Fig. S1). The variation of rhodamine concentration was monitored over time by UV–Vis spectroscopy. The NFs of PCL, CS-PCL, TiO_2NPs/CS-PCL and TiO_2NPs/PCL were compared to observe the effect of the different components on degradation.

The second method followed the photodegradation through fluorescence microscopy, studying the decoloration of RhB against two sources of radiation: UV light (LED 365 nm) and blue light (LED 460 nm). For this purpose, a 1 cm^2 piece mat was immobilized on a glass slide, using a double-sided adhesive tape that served as a fixative and spacer for the samples. An adhesive frame was fabricated to adhere and stretch the mat's edges on the slide while providing a controlled and closed environment with a second slide placed on top of the sample. Prior to the application of the second slide and fluorescence measurements, 10 μL of 2×10^{-5} M aqueous RhB solution was added to the stretched mat surface.

3. Results and discussion

3.1. Nanofibers fabrication and characterization

In order to obtain continuous, uniform, and bead-free NFs an optimization of the electrospinning parameters was performed. The optimization was carried out by systematically adjusting the solution conditions (solvent, solution concentration, and CS:PCL ratio) and processing parameters (voltage, needle tip-to-collector distance, and flow rate). A scheme with the main conditions tested and the obtained results is reported in Fig. S2.

Although some reported results show that CS can be electrospun using trifluoroacetic acid as a solvent [39], in order to use less aggressive conditions, in the present work a mixture of acetic acid and formic acid was selected as solvent for the electrospinning of CS-PCL blends [30]. The effectiveness of the electrospinning process was assessed by checking the Taylor cone formation at the needle tip and the stable ejection of a single jet. To study nanofibers formation, first, a solution containing PCL at 8%wt was investigated varying the CS:PCL ratio from 10:90 to 20:80. The solution with the highest CS content (20:80) presented too high viscosity, which prevented carrying out the electrospinning process. The CS-PCL blend solutions with lower CS content (10:90 and 15:85) allowed electrospinning at different voltages and flow rates. However, both solutions presented very low jet stability and low process reproducibility. Fig. S3A-F shows fibers obtained under these

conditions. All electrospinning tests were repeated by decreasing the PCL concentration to 6%wt, as indicated in the schematic in Fig. S2, the obtained NFs are shown in Fig. S3G-L. The decrease in viscosity of the resulting solutions substantially improved their processability for obtaining NFs. In addition, the effect of CS on the electrospinning process was evident, with a higher amount of CS, the jetting stability decreased drastically. Notably, the use of a polymer solution containing 6%wt PCL and a CS:PCL ratio of 10:90 proved to be particularly effective for the production of nanofibers with good morphology, by using the following optimized processing conditions: operating voltage 19 kV, collector-to-needle distance 12.5 cm, and flow rate 0.6 mL/h.

Fig. 1(A-C) shows SEM micrographs and the respective fiber diameter distribution of PCL, CS-PCL and TiO_2/CS-PCL electrospun mats obtained with these optimized experimental parameters. Uniform and bead-free NFs were observed with mean diameter of 190 ± 48, 126 ± 41 and 139 ± 45 nm for PCL, CS-PCL and TiO_2/CS-PCL respectively. Both blends with CS exhibit ultrafine spiderweb-like fibers (≤ 40 nm) between the main fibers. This phenomenon is attributed to CS presence, in agreement with other reported results [26]. The decrease in mean fibers diameter when CS was added would be mainly due to strong repulsive forces between ionogenic groups within the polyelectrolyte backbone which imposes higher elongation forces leading to thinner fibers, as described in the literature [40]. On the other hand, when the TiO_2NPs are added, the viscosity of the solution increases causing a slight increase in the fibers mean diameter compared to CS-PCL fibers [33].

TiO_2/CS-PCL NFs presented a surface with TiO_2 NPs aggregates of 20 to 40 nm in various zones of the NFs, as can be observed in the SEM image of the mat without gold coating (Fig. 1D) where the TiO_2 NPs are distinguishable by their higher brightness. The TEM image of a single TiO_2/CS-PCL fiber confirms the presence of the NPs (Fig. 1E).

The surface wettability of the electrospun mats was evaluated through water contact angle (WCA) measurements. The WCA values determined for the CS-PCL and TiO_2/CS-PCL mats were 82 ± 6° and 90 ± 10° respectively. An overall reduction of the WCA with respect to plain PCL electrospun membrane (PCL NFs: 188 ± 5° [41]) was obtained, these was attributed to the presence of CS in the NFs, which increases the polar contribution of the material [42]. The decrease in the contact angle of the mats yields significant advantages for the adsorption and degradation processes of organic contaminants. Given the contaminant presence in aqueous medium, this reduction facilitates the unobstructed water flow throughout the intricate three-dimensional framework, thereby enhancing the mobility of the contaminants. Furthermore, the moderate angle attained plays a pivotal role in promoting the adsorption of organic contaminants, capitalizing on their inherent amphiphilic chemical characteristics.

The chemical composition of the electrospun mats was studied by FTIR spectroscopy. Fig. 2 shows FTIR spectra of PCL, CS-PCL, and TiO_2/CS-PCL NFs, as well as the spectrum of a CS film (prepared by solvent casting from acetic acid 1 %*V*/V) for comparative purposes. The absorption bands of PCL attributed to the asymmetric and symmetric stretching vibration of CH_2 were located at 2945 and 2865 cm^{-1}, respectively; the signal corresponding to the stretching of CO in the ester

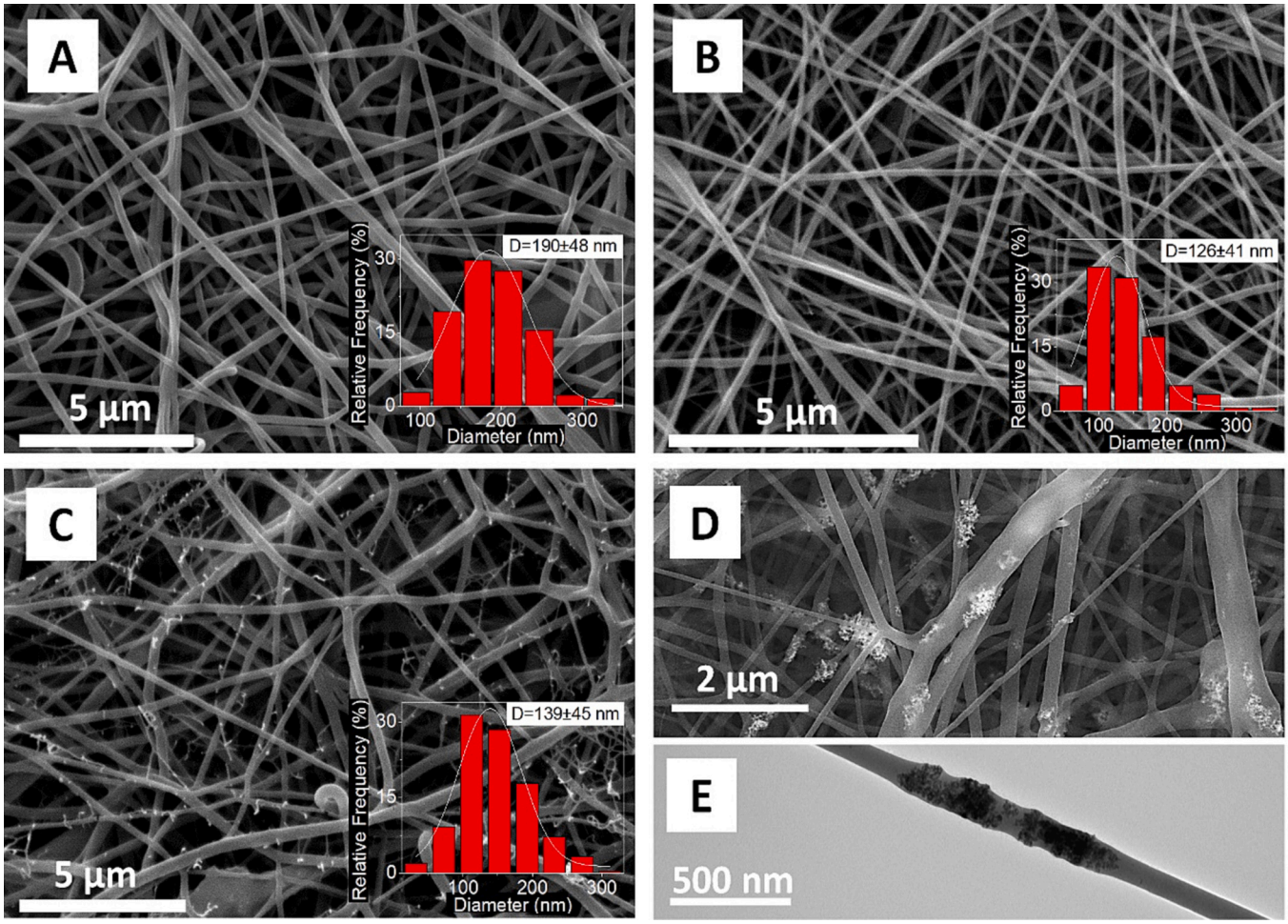

Fig. 1. SEM micrographs of electrospun mats: (A) PCL, (B) CS-PCL, (C) TiO_2/CS-PCL. Insets show the corresponding fiber diameter distribution. (D) SEM Image of TiO_2/CS-PCL mat not coated with gold. (E) TEM image of a single fiber of TiO_2/CS-PCL. (For interpretation of the references to colour in this figure legend, the reader is referred to the web version of this article.)

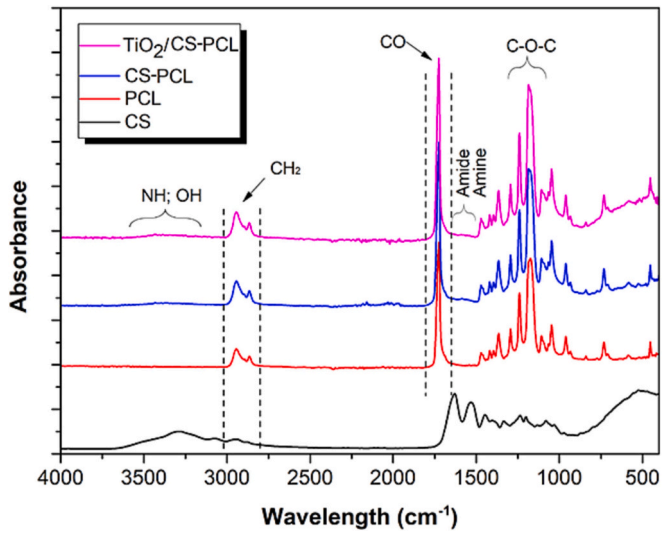

Fig. 2. FT-IR spectra of PCL, CS-PCL, TiO_2/CS-PCL electrospun mats and a CS film.

group appears at 1726 cm^{-1}; while the signals of the asymmetric and symmetric stretching vibrations of C-O-C appear at 1240 and 1175 cm^{-1} [36]. In the spectra of CS-containing NFs, characteristic CS bands with very low absorbance were observed, a band near 3441 cm^{-1} corresponding to the stretching vibration of the NH and OH groups and others at 1545 and 1630 cm^{-1} for the amine and amide groups of CS. [43]. Despite its low intensity in these zones, a clear absorbance difference can be observed in the spectra concerning neat PCL NFs, as reported for similar systems [44]. A significant increase in absorbance was also observed in the range of 400 to 700 cm^{-1} which corresponds to the characteristic band of TiO_2 [45]. No significant changes were detected in the wavelength of the signals corresponding to PCL due to the incorporation of TiO_2 NPs, which would indicate that there is a weak interaction between PCL and NPs. On the other hand, due to the low absorbance of the CS signals, it was not possible to evaluate wavelength shifts of these signals that could indicate the interaction of CS with the NPs.

The thermal degradation profiles obtained by thermogravimetric analysis (TGA) along with the respective derived curves of CS film and PCL, CS-PCL, TiO_2/CS-PCL NFs are shown in Fig. 3 A and B, and some parameters determined from these are summarized in Table 1. PCL degrades with a single weight loss step at a temperature of maximum degradation rate (T_{max}) of 428 °C, in agreement with the literature, where a double simultaneous mechanism, random chain scission and

Table 1
Thermogravimetric results of the investigated materials: temperature of maximum degradation rate (T_{max}) and residual weight at 600 °C.

Sample	T_{max} (°C)		Residue (%) at 600 °C
CS	320	–	39
PCL	–	428	5
CS-PCL	300	427	8
TiO_2/CS-PCL	305	428	12

specific chain end scission, is proposed [46,47]. On the other hand, CS shows a first weight loss in the range from room temperature to around 150 °C due to water evaporation, and a main degradation step at a T_{max} of 320 °C, in agreement with literature data [48]. It is worth noting that CS is characterized by a high residue (39 %) at 600 °C. The CS-PCL electrospun blends, showed two distinct weight loss steps at temperatures characteristic of the two single polymers (Fig. 3 and Table 1), respectively assigned to thermal degradation of PCL and CS.

It is worth noting that no considerable change in the degradation temperatures of the materials was observed upon the addition of TiO_2 NPs, most likely due to the relatively small amount of the NPs in the material.

The residual weight percentages after degradation of the polymeric matrix (at 600 °C) were used to determine the amount of TiO_2 NPs in samples [49]. It was possible to calculate the inorganic TiO_2 content using the Eqs. (2) and (3). However, it was necessary to evaluate the thermograms excluding the initial weight loss due to water and the carbonaceous residue remaining at the end. The residual weight at 600 °C was taken to calculate the composition of the polymer blends. The actual CS:PCL and CS:PCL:TiO_2 ratios were determined to be 9:91 (w/w) and 8:88:4 (w/w/w) respectively.

Differential scanning calorimetry (DSC) thermograms of nanofibrous mats are shown in Fig. 4A. The investigated materials exhibited sharp endothermic peaks at 58, 60 and 59 °C for PCL, CS-PCL and TiO_2/CS-PCL NFs respectively, which can be attributed to the melting of the semicrystalline polymer PCL, while chitosan film showed no signals in the analysed temperature range.

Fig. 4B summarizes the crystallinity degree (χ_c%) of each material in the three different heating scans. The first cycle corresponds to the material as it was obtained from the electrospinning process. The second cycle is after a controlled cooling, and the last is after quench cooling, as described in the Materials and Methods section. From the χ_c% values, it can be inferred that the spinning process favours PCL crystallization leading to considerably higher χ_c% values. It should be noted that the highest value of χ_c% was obtained for the mat containing TiO_2 NPs, which may indicate a relatively good distribution of the NPs in the material that have been demonstrated to influence the behaviour of

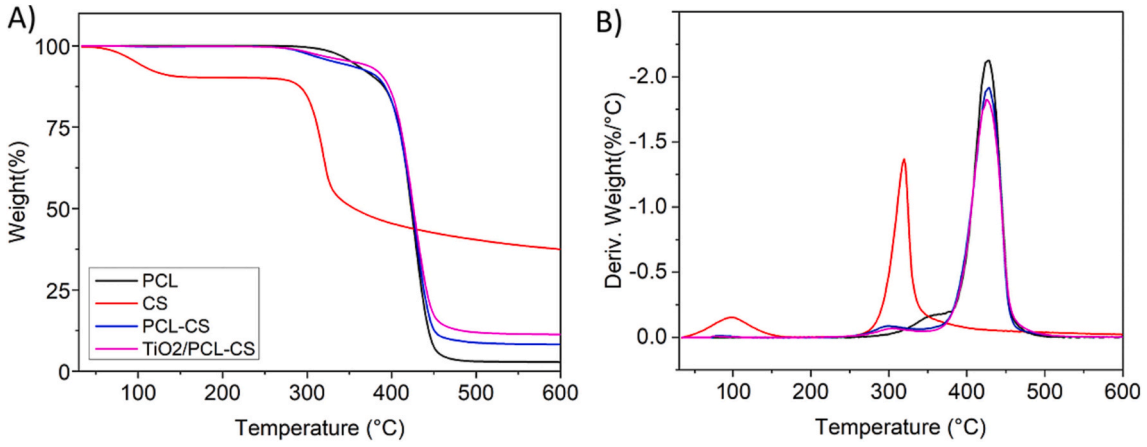

Fig. 3. A) TGA and B) DTG curves of PCL, CS-PCL, TiO_2/CS-PCL electrospun mats and a CS film.

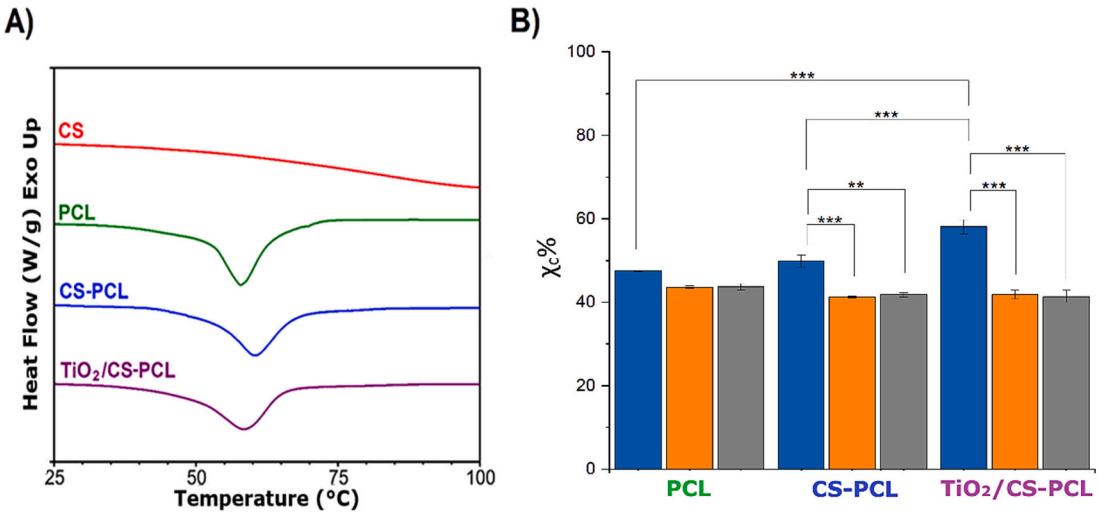

Fig. 4. A) DSC thermograms of PCL, CS-PCL, TiO_2/CS-PCL electrospun mats, and a CS film (first heating scan). B) Crystallinity degree (χ_c%) of each material in three heating cycles. Blue: first cycle; Orange: second cycle; Gray: third cycle. * $p \leq 0.05$ ** $p \leq 0.01$ *** $p \leq 0.001$. (For interpretation of the references to colour in this figure legend, the reader is referred to the web version of this article.)

semicrystalline polymers [50,51].

The effect of TiO_2 NPs on the mechanical properties of NFs was studied based on stress-strain curves. Fig. S4 shows representative results for the two CS-PCL, and TiO_2/CS-PCL NFs, whereas Table 2 summarizes the mean values of tensile stress (σ_b), elongation at break (ε_b), and Young's modulus (E). It was observed that the tensile properties of CS-PCL NFs were slightly improved by adding the TiO_2 NPs, with an increase in σ_b from 66 to 86 MPa. However, no significant difference was observed in the Young's modulus and elongation at break. In a related study conducted by Lim et al. [52], which explored the influence of fibers diameter on mechanical properties of PCL nanofibers in similar conditions, it was found that as the fibers diameter decreased, both the Young's modulus (E) and tensile strength (σ_b) increased. The authors reported that PCL fibers with a diameter near to 200 nm displayed a modulus of around 1000 MPa and σ_b of 380 Pa. Those values are considerable higher that the obtained for our materials with the incorporation of CS and TiO_2NPs. In literature, there are reports where the CS had the same effect in the mechanical properties [53]. While the incorporation of TiO_2 into polymer matrices has consistently demonstrated a substantial enhancement in elastic modulus and mechanical properties, attributed to TiO_2 remarkable high elastic modulus, typically ranging from 300 to 320 GPa [54]. However, in our material, the agglomeration of nanoparticles during the electrospinning process could potentially impede the anticipated improvement in these properties.

To know the porosity and pore distribution of the nanofibrous assembly, the N_2 adsorption-desorption technique was used. N_2 adsorption-desorption isotherms for the BET analysis and Barrett-Joyner-Halenda (BJH) pore size distribution are shown in Fig. S5. According to the IUPAC classification, in all cases, type II isotherms are observed with a hysteresis loop at high relative pressure, which is characteristic of a material with a wide range of mesopore sizes extending into the macropore range [55]. BJH pore size distribution plots (Fig. S5D—F) show that the pore distribution is quite heterogeneous, as expected from a material composed of interlaced NFs.

Table 3 summarizes the specific surface area for the electrospun mats. The PCL mat presented the lowest specific surface area, followed by CS-PCL and finally by TiO_2/CS-PCL, the latter presenting the highest total pore volume. This means that the NFs-NPs hybrid material presents a larger area to interact with the medium, which potentially favours adsorption processes. These results correspond to the fiber diameters found through morphological analysis, following the trend that the smaller the fiber diameter, the larger surface area.

Table 2
Tensile properties of electrospun mats.

Sample	E (MPa)	ε_b(%)	σ_b (MPa)
CS-PCL	384 ± 92	75 ± 8	66 ± 8
TiO_2/CS-PCL	393 ± 85	65 ± 10	86 ± 10

Table 3
Specific surface area and total pore volume for electrospun mats obtained from N_2 adsorption-desorption isotherms.

Mat	Specific surface BET (m^2/g)	Total pore volume (cm^3/g) x10 ^{2}	Adsorption per area (mg/m^2) x10 ^{2}
PCL	10.12 ± 0.02	3.27	1.28
CS-PCL	13.81 ± 0.07	3.23	3.04
TiO_2/CS-PCL	15.28 ± 0.03	4.57	7.53

3.2. Study of Rhodamine B adsorption capacity by the electrospun nanofibers

Adsorption properties of the electrospun NFs were studied through

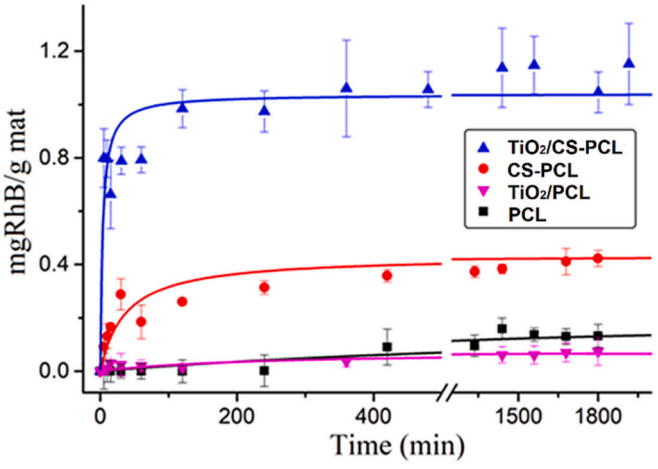

Fig. 5. Effect of contact time on the adsorption capacity of RhB, for PCL, CS-PCL, TiO_2/PCL, and TiO_2/CS-PCL nanofibers.

batch-type experiments by contacting electrospun mats with RhB solution. Fig. 5 illustrates the adsorption capacity of PCL, TiO_2/PCL, CS-PCL and TiO_2/CS-PCL mats with respect to contact time with the RhB solution. It can be observed that for PCL and TiO_2/PCL NFs no appreciable RhB adsorption is obtained, having maximum adsorption of around 0.13 mg RhB per gram of mat after 30 h. While for CS-PCL and TiO_2/CS-PCL, the adsorption curves suggest that the dye binding to active sites had a significant increase up to 90 min and stabilized around 180 min (3 h), with maximum adsorption of around 0.42 and 1.15 mg RhB/g mat for CS-PCL and TiO_2/CS-PCL, respectively. In this regard, the adsorption capacity of NFs increased in the order PCL ~ TiO_2/PCL < CS-PCL < TiO_2/CS-PCL.

Using the surface area obtained by BET, adsorption capacity per unit area was calculated. The adsorption values per unit area is summarized in Table 3. TiO_2/CS-PCL NFs is the material with the highest amount of RhB adsorbed per gram of mat follow by CS-PCL and PCL NFs. The adsorption per area values showed that the increase in adsorption was not caused by the increase in the surface area of the NFs but by their composition. Remarkably, the presence of CS in NFs increased the RhB adsorption almost three times, while TiO_2NPs did not show a change in adsorption between PCL and PCL-TiO_2 NFs. Furthermore, when CS and TiO_2NPs are present at the same time, the adsorption per area of RhB increases to 7.53×10^{-2} mg/m^2 which is not explained by the sum of independent adsorption of each component. Thus, this increase can be attributed to a synergistic effect between them. This effect could be explained considering that CS can attract the contaminant molecules to NFs, i.e. to the vicinity of active adsorption sites, such as TiO_2NPs surface and other CS molecules, increasing their maximum capacity, evidencing the phenomenon known as a bait-hook effect. In contrast, PCL NFs and PCL-TiO_2 NFs do not show this RhB adsorption which means that TiO_2NPs has a lower capacity to attract RhB from the solution bulk.

All the results suggest that the adsorption of RhB on the surface of NFs adheres to a pseudo-second order model, highlighting the significance of a chemical reaction or chemisorption between RhB and NFs in the rate-limiting step of the adsorption process. Moreover, the intraparticle diffusion mechanism involved in this adsorption process exhibits two distinct stages: macropore diffusion and micropore diffusion. Initially, RhB molecules traverse through the larger pores present in the adsorbent (macropore diffusion), followed by their diffusion into the smaller pores (micropore diffusion). Both of these stages play crucial roles in the overall adsorption process. For a more comprehensive analysis and detailed information, refer to Appendix 1 in the SI.

3.3. Study of photocatalytic activity of rhodamine B degradation of electrospun mats followed by fluorescence microscopy

In order to evaluate the photoactivity of the fibers, RhB was deposited on the fibers and its degradation was evaluated by fluorecence microscopy under UV irradiation (365 nm). The time-dependent decoloration of RhB under this irradiation is shown in Fig. 6 where it can be observed that CS-PCL NFs present a slight decoloration, i.e. low RhB degradation, while TiO_2/CS-PCL NFs present a much more dramatic photodegradation activity. The above verifies that the photocatalytic properties of TiO_2 are maintained after the electrospinning process.

To quantify and compare the photoactivity data of our materials, these results were linearly adjusted, obtaining pseudo-zero-order kinetics. Pseudo-zero-order kinetics was possibly due to the measurement strategy, where the NFs are saturated with dye, and the excitation radiation directly impacts the material, leading to this kinetic model [56]. TiO_2/CS-PCL NFs presented a higher rate constant for RhB photodegradation; this could be connected with the fact that TiO_2NPs exhibited good stability in the polymeric solution.

The photocatalytic reaction of TiO_2/CS-PCL NFs starts when TiO_2NPs absorb the energy from the radiation source. The photonic excitation then leaves the valence band (VB) unfilled, creating the

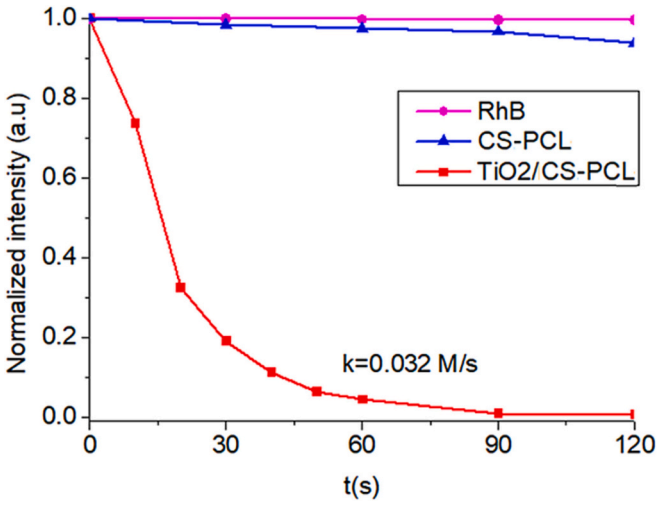

Fig. 6. Photocatalytic activity of CS-PCL and TiO_2/CS-PCL NFs for RhB degradation under UV radiation.

electron-hole pair (e–h+). Excited electrons in the conduction band (CB) can flow to or from the absorber, allowing the formation of both positively and negatively charged species on the surface [57]. In general, the electron in CB moves towards the surface and it is scavenged by the oxygen in the medium to generate the superoxide anion $O_2\cdot^-$, which can become the radical HOO· by rapidly protonation, simultaneously the h^+ in the VB migrates through NP surface and reacts with both H_2O and OH^- ions to produce active species such as OH·. It is important to note that the processes efficiency can be attributed to the efficient separation of photogenerated e^--h^+ pairs. Thus, the active oxygen species ($O_2\cdot^-$, HOO·, OH·) are responsible for the degradation of RhB into less harmful minerals or organic compounds [57–61].

3.4. Study of photocatalytic activity of electrospun mats under visible irradiation in batch-type experiments

Photocatalytic activity of the electrospun mats was also evaluated by degradation of an RhB aqueous solution using a white LED light (2900–3000 K). These experiments allowed the study of the photocatalysis phenomenon in a system closer to sunlight and each component's effect on degradation.

In this regard, Fig. 7 shows UV–Vis spectra of aqueous solutions of RhB over time for NFs of TiO_2/CS-PCL and TiO_2/PCL (in the absence of chitosan). The colour of the curves allows visualization of the main effects at each stage of the experiment, from violet curves (t 0 h) through red curves (t 24 h) to blue curves (t 95 or 120 h).

For both systems, RhB solution in the presence of the electrospun materials shows two noticeable changes, one corresponding to a decrease in absorbance and the other to a hypsochromic shift in the maximum absorbance. In the first stage (violet to pink curves), a decrease in the main absorption band at 560 nm is observed, while in the second stage (red to yellow curves), the hypsochromic shift is mainly observed, and in the final stage (blue curves) a prolonged decrease in the absorbance of the band at 498 nm continues. It should be noted that throughout the experiment, both changes occur simultaneously.

The loss in absorbance can be attributed to the dye chromophore destruction, and the blue shift is due to N-deethylation of RhB, with the product being rhodamine (λ_{max} 498 nm) [62]. This indicates that the degradation pathway proceeded through forming a series of N-deethylated intermediates during the photodegradation reaction process [63]. In addition, a significant change in the reaction rate between rhodamine and RhB is observed, drastically prolonging the reaction times.

Since TiO_2 does not absorb in the visible light range, the semiconductor's role is different in this case. Instead of being directly excited

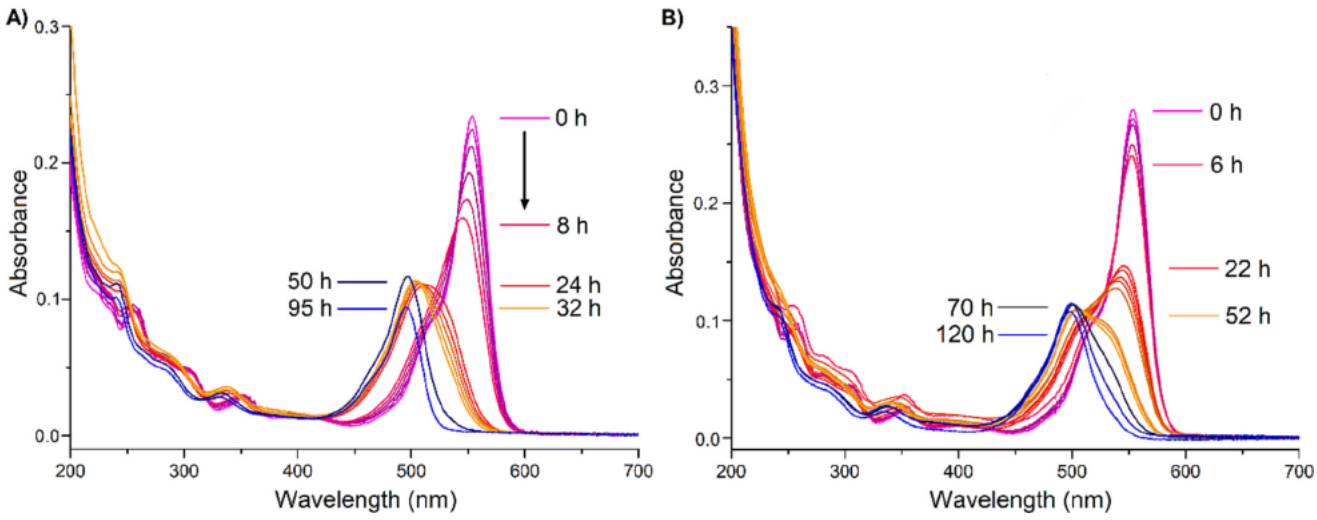

Fig. 7. UV–Vis absorption spectra of aqueous solutions of RhB during irradiation. A) TiO_2/CS-PCL; B) TiO_2/PCL.

by light, the dye absorbs the light and is excited; this electron is transferred to the semiconductor and finally to the electron-accepting substances [64]. In other words, the main character as a dye, its strong visible-light absorption, is exploited to initiate TiO_2-catalyzed removal of RhB. The interaction between the dye and the TiO_2NPs is indispensable for efficiently injecting photoinduced electrons and subsequent degradation reactions. RhB is known to bind to the TiO_2 surface via esterification between the carboxylic group of dye and the hydroxylated TiO_2 surface [64].

There are two possible routes for electron transfer from the dye to the semiconductor. The first is an injection from the excited state (singlet or triplet) of the dye to the conduction band of TiO_2, and the second, is favoured by strong coupling of the π orbital of the dye with the 3d orbital of Ti, which forms a charge transfer complex; thus a charge transfer from ligand to metal (LMCT) occurs, promoting an electron from the basal state of the complex to the conduction band of TiO_2 [64].

When the RhB concentration approaches zero, the degradation rate of rhodamine decreases drastically due to the loss of electron injection capacity from an excited state, as the led light used presents an emission minimum at around 500 nm, corresponding to the absorbance maximum of rhodamine.

The kinetic expression most commonly used to explain heterogeneous catalytic processes is the Langmuir-Hinshelwood (LH) kinetic model [65], and LH kinetics can be reduced to first-order kinetics [56,66], resulting in the following equation:

$$ln\left(\frac{C}{C_0}\right) \quad k_1 t \tag{4}$$

Where C is the dye concentration at any time during degradation, k_1 $k_{cat}K$, K is the equilibrium constant for the adsorption of the substrate onto the catalyst and k_{cat} degradation reaction constant rate. In other words, the degradation kinetics depend on pollutant concentration, while TiO_2 concentration acts as a constant [22].

Fig. 8 shows the evolution of RhB concentration as a function of experiment time in the presence of PCL, CS-PCL, TiO_2/PCL, and TiO_2/CS-PCL NFs.

In presence of PCL and CS-PCL NFs, a small decrease in the concentration of RhB was observed. However, there was no appreciable differentiation from the blank (RhB alone), i.e., neither CS nor PCL had the capacity to degrade RhB.

TiO_2/CS-PCL and TiO_2/PCL fit the first-order kinetic model very well with R^2 values of 0.99826 and 0.98374, respectively. Meanwhile, k_1 values of 10.09×10^{-4} and 4.36×10^{-4} min^{-1} were obtained for the systems with and without CS, respectively. The rate constant for the NFs

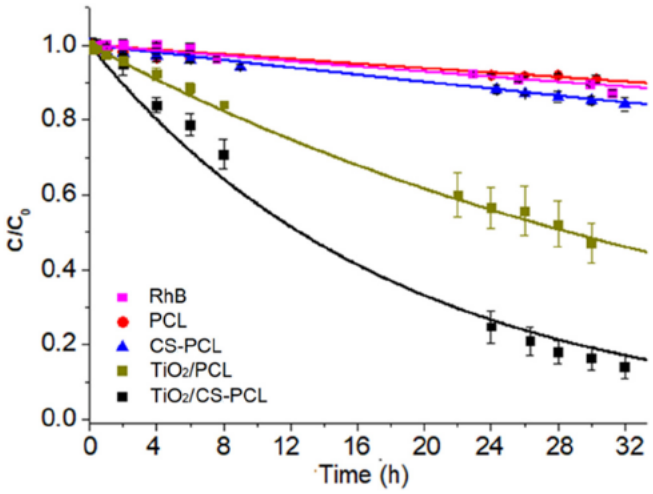

Fig. 8. Photocatalytic degradation of RhB by PCL, CS-PCL, TiO_2/PCL and TiO_2/CS-PCL NFs. Each point represents the mean of three replicates, while the error bars the associated error. A solution of RhB was used as the degradation blank.

with CS is more than double compared to the NFs without CS. This demonstrates the importance of CS in the decolorization process. CS would attract the dye to the vicinity of the catalyst's active sites, favouring its faster degradation.

In this way, the decolorization process can be divided into two distinct stages. The initial step involves the adsorption process, where CS effectively attracts and captures pollutants. Following this, the second stage entails the photodegradation process facilitated by the ROS generated by TiO_2NPs, as illustrated in Fig. 9.

4. Conclusions

The preparation of electrospun nanofibers from mixtures of chitosan and polycaprolactone was optimized and TiO_2 NPs were successfully incorporated into the polymer matrix. The study of the adsorption capacity and photocatalytic activity of the materials against rhodamine B as a model compound showed that chitosan played a key role in the results obtained. The adsorption capacity of RhB by the nanocomposites was strongly affected by the composition of the mats. CS significantly favoured the adsorption of RhB, and a synergistic effect on adsorption was observed when CS and TiO_2 NPs were simultaneously present in the

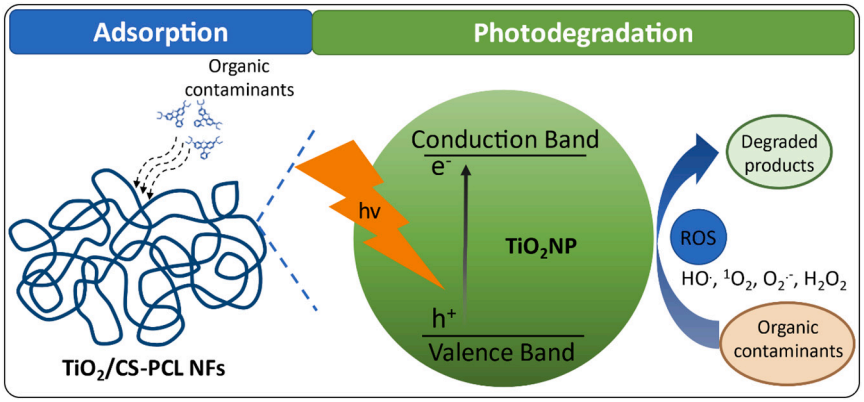

Fig. 9. Diagram of the mechanism of decolorization process by TiO_2/CS-PCL NFs.

NFs. In addition, the hybrid NFs containing chitosan (TiO_2/CS-PCL) presented the highest rate constant for the photodegradation of RhB. From these results, it can be inferred that CS attracts the contaminant from the surrounding medium to the active sites within the NFs, including other CS molecules and TiO_2NPs, facilitating both adsorption and subsequent degradation. Accordingly, a so-called bait-hook-and-destruct effect was evidenced in the process. The important contribution made by chitosan in the degradation of an organic dye in water reported in this work, allows projecting a high potentiality and very good performance of catalytic and especially photocatalytic hybrid nanomaterials containing chitosan (and probably also other biopolymers) in different areas.

CRediT authorship contribution statement

Alexander Cordoba: Conceptualization, Methodology, Formal analysis, Investigation, Writing - Original Draft.

Moreno Guernelli: Investigation, Formal analysis.

Marco Montalti: Methodology, Supervision, Writing - Review.

Cesar Saldías: Methodology, Supervision, Writing - Review.

Maria Letizia Focarete: Conceptualization, Methodology, Supervision, Writing - Review & Editing.

Angel Leiva: Conceptualization, Methodology, Supervision, Writing - Review & Editing, Funding acquisition.

Declaration of competing interest

The authors declare that they have no known competing financial interests or personal relationships that could have appeared to influence the work reported in this paper.

Data availability

Data will be made available on request.

Acknowledgements

A.C. thanks the doctoral scholarship ANID 2019-21191257, A.L. thanks to FONDECYT 1211124 and FONDAP 1522A0006 projects.

Appendix A. Supplementary data

Supplementary data to this article can be found online at https://doi.org/10.1016/j.ijbiomac.2023.127111.

References

[1] A. Boretti, L. Rosa, Reassessing the projections of the world water development report, Clean Water 2 (1) (2019) 15.

[2] A.R. Ribeiro, O.C. Nunes, M.F. Pereira, A.M. Silva, An overview on the advanced oxidation processes applied for the treatment of water pollutants defined in the recently launched Directive 2013/39/EU, Environ. Int. 75 (2015) 33–51.

[3] D.B. Miklos, C. Remy, M. Jekel, K.G. Linden, J.E. Drewes, U. Hübner, Evaluation of advanced oxidation processes for water and wastewater treatment–a critical review, Water Res. 139 (2018) 118–131.

[4] M.R. Hoffmann, S.T. Martin, W. Choi, D.W. Bahnemann, Environmental applications of semiconductor photocatalysis, Chem. Rev. 95 (1) (1995) 69–96.

[5] S.H. Szczepankiewicz, A. Colussi, M.R. Hoffmann, Infrared spectra of photoinduced species on hydroxylated titania surfaces, J. Phys. Chem. B 104 (42) (2000) 9842–9850.

[6] A. Khataee, M.B. Kasiri, Photocatalytic degradation of organic dyes in the presence of nanostructured titanium dioxide: influence of the chemical structure of dyes, J. Mol. Catal. A Chem. 328 (1–2) (2010) 8–26.

[7] C. Weiss, M. Carriere, L. Fusco, I. Capua, J.A. Regla-Nava, M. Pasquali, J.A. Scott, F. Vitale, M.A. Unal, C. Mattevi, Toward nanotechnology-enabled approaches against the COVID-19 pandemic, ACS Nano 14 (6) (2020) 6383–6406.

[8] P.V.L. Reddy, B. Kavitha, P.A.K. Reddy, K.-H. Kim, TiO2-based photocatalytic disinfection of microbes in aqueous media: a review, Environ. Res. 154 (2017) 296–303.

[9] A. Habibi-Yangjeh, S. Asadzadeh-Khaneghah, S. Feizpoor, A. Rouhi, Review on heterogeneous photocatalytic disinfection of waterborne, airborne, and foodborne viruses: can we win against pathogenic viruses? J. Colloid Interface Sci. 580 (2020) 503–514.

[10] T. Watanabe, T. Takizawa, K. Honda, Photocatalysis through excitation of adsorbates. 1. Highly efficient N-deethylation of rhodamine B adsorbed to cadmium sulfide, J. Phys. Chem. 81 (19) (1977) 1845–1851.

[11] S.N. Frank, A.J. Bard, Heterogeneous photocatalytic oxidation of cyanide and sulfite in aqueous solutions at semiconductor powders, J. Phys. Chem. 81 (15) (1977) 1484–1488.

[12] Q. Guo, C. Zhou, Z. Ma, X. Yang, Fundamentals of TiO2 Photocatalysis: concepts, mechanisms, and challenges, Adv. Mater. 31 (50) (2019) 1901997.

[13] J.J. Rueda-Marquez, I. Levchuk, P. Fernández Ibanez, M. Sillanpaa, A critical review on application of photocatalysis for toxicity reduction of real wastewaters, J. Clean. Prod. 258 (2020) 120694.

[14] S. Singh, H. Mahalingam, P.K. Singh, Polymer-supported titanium dioxide photocatalysts for environmental remediation: a review, Appl. Catal. A Gen. 462-463 (2013) 178–195.

[15] A. Cordoba, C. Saldias, M. Urzúa, M. Montalti, M. Guernelli, M.L. Focarete, A. Leiva, On the versatile role of electrospun polymer nanofibers as photocatalytic hybrid materials applied to contaminated water remediation: a brief review, Nanomaterials 12 (5) (2022).

[16] D. Ding, Z. Li, S. Yu, B. Yang, Y. Yin, L. Zan, N.V. Myung, Piezo-photocatalytic flexible PAN/TiO2 composite nanofibers for environmental remediation, Sci. Total Environ. 824 (2022) 153790.

[17] Y. Ma, D. He, J. Liu, Y. Wang, M. Yang, H. Wang, J. Qiu, W. Li, Y. Li, C. Wang, Adsorption and visible light photocatalytic degradation of electrospun PAN@W18O49 nanofibers, Chem. Res. Chin. Univ. 37 (3) (2021) 428–435.

[18] P. Teng, Z. Li, S. Gao, K. Li, N. Copner, L. Zhihai, X. Yang, Flexible PAN-BiOI-AgI heterojunction nanofiber and the photocatalytic degradation property, Opt. Mater. Express 12 (3) (2022) 1031–1042.

[19] G. Panthi, K.R. Gyawali, M. Park, Towards the enhancement in photocatalytic performance of Ag3PO4 nanoparticles through sulfate doping and anchoring on electrospun nanofibers, Nanomaterials 10 (5) (2020).

[20] Z. Huang, Z. Lai, D. Zhu, H. Wang, C. Zhao, G. Ruan, F. Du, Electrospun graphene oxide/MIL-101(Fe)/poly(acrylonitrile-co-maleic acid) nanofiber: a high-efficient and reusable integrated photocatalytic adsorbents for removal of dye pollutant from water samples, J. Colloid Interface Sci. 597 (2021) 196–205.

[21] F. Sun, S.-Y. Huang, H.-T. Ren, T.-T. Li, Y. Zhang, C.-W. Lou, J.-H. Lin, Core-sheath structured TiO2@PVDF/PAN electrospun membranes for photocatalysis and oil-water separation, Polym. Compos. 41 (3) (2020) 1013–1023.

[22] L. Lou, J. Wang, Y.J. Lee, S.S. Ramkumar, Visible light photocatalytic functional TiO2/PVDF nanofibers for dye pollutant degradation, Part. Part. Syst. Charact. 36 (9) (2019) 1900091.

[23] P. Pascariu, C. Cojocaru, P. Samoila, N. Olaru, A. Bele, A. Airinei, Novel electrospun membranes based on PVDF fibers embedding lanthanide doped ZnO for adsorption and photocatalytic degradation of dye organic pollutants, Mater. Res. Bull. 141 (2021) 111376.

[24] A. Gupta, N. Khosla, V. Govindasamy, A. Saini, K. Annapurna, S.R. Dhakate, Trimetallic composite nanofibers for antibacterial and photocatalytic dye degradation of mixed dye water, Appl. Nanosci. 10 (11) (2020) 4191–4205.

[25] P. Pascariu, L. Olaru, A.L. Matricala, N. Olaru, Photocatalytic activity of ZnO nanostructures grown on electrospun CAB ultrafine fibers, Appl. Surf. Sci. 455 (2018) 61–69.

[26] L. Van der Schueren, T. De Meyer, I. Steyaert, O. Ceylan, K. Hemelsoet, V. Van Speybroeck, K. De Clerck, Polycaprolactone and polycaprolactone/chitosan nanofibres functionalised with the pH-sensitive dye Nitrazine Yellow, Carbohydr. Polym. 91 (1) (2013) 284–293.

[27] S. Haider, S.-Y. Park, Preparation of the electrospun chitosan nanofibers and their applications to the adsorption of Cu(II) and Pb(II) ions from an aqueous solution, J. Membr. Sci. 328 (1) (2009) 90–96.

[28] F. Ajalloueian, H. Tavanai, J. Hilborn, O. Donzel-Gargand, K. Leifer, A. Wickham, A. Arpanaei, Emulsion Electrospinning as an Approach to Fabricate PLGA/Chitosan Nanofibers for Biomedical Applications, BioMed Research International, 2014, p. 475280.

[29] N. Bhattarai, Z. Li, J. Gunn, M. Leung, A. Cooper, D. Edmondson, O. Veiseh, M.-H. Chen, Y. Zhang, R.G. Ellenbogen, M. Zhang, Natural-synthetic polyblend nanofibers for biomedical applications, Adv. Mater. 21 (27) (2009) 2792–2797.

[30] L. Van der Schueren, I. Steyaert, B. De Schoenmaker, K. De Clerck, Polycaprolactone/chitosan blend nanofibres electrospun from an acetic acid/formic acid solvent system, Carbohydr. Polym. 88 (4) (2012) 1221–1226.

[31] S. Karagoz, N.B. Kiremitler, M. Sakir, S. Salem, M.S. Onses, E. Sahmetlioglu, A. Ceylan, E. Yilmaz, Synthesis of Ag and TiO2 modified polycaprolactone electrospun nanofibers (PCL/TiO2-Ag NFs) as a multifunctional material for SERS, photocatalysis and antibacterial applications, Ecotoxicol. Environ. Saf. 188 (2020) 109856.

[32] H. Tu, D. Li, Y. Yi, R. Liu, Y. Wu, X. Dong, X. Shi, H. Deng, Incorporation of rectorite into porous polycaprolactone/TiO2 nanofibrous mats for enhancing photocatalysis properties towards organic dye pollution, Compos. Commun. 15 (2019) 58–63.

[33] M. Karthega, M. Pranesh, C. Poongothai, N. Srinivasan, Poly caprolactone/titanium dioxide nanofiber coating on AM50 alloy for biomedical application, J. Magnesium Alloys 9 (2) (2021) 532–547.

[34] S. Ahmadi, Y. Pilehvar, N. Zarghami, A. Abri, Efficient osteoblastic differentiation of human adipose-derived stem cells on TiO2 nanoparticles and metformin co-embedded electrospun composite nanofibers, J. Drug Deliv. Sci. Technol. 66 (2021) 102798.

[35] M. Hadjianfar, D. Semnani, J. Varshosaz, S. Mohammadi, S.P. Rezazadeh Tehrani, 5FU-loaded PCL/Chitosan/Fe_3O_4 core-shell nanofibers structure: an approach to multi-mode anticancer system, Adv. Pharm. Bull. 12 (3) (2022) 568–582.

[36] Z. Amini, S.S. Rudsary, S.S. Shahraeini, B.F. Dizaji, P. Goleij, A. Bakhtiari, M. Irani, F. Sharifianjazi, Magnetic bioactive glasses/Cisplatin loaded-chitosan (CS)-grafted-poly (ε-caprolactone) nanofibers against bone cancer treatment, Carbohydr. Polym. 258 (2021) 117680.

[37] C. Sun, D. He, Y. Qi, G. Zhang, Q. Huang, Spectroscopic characterization of a polycaprolactone-chitosan electrospun scaffold modified with photocatalytic TiO2 nanoparticles for improved wound healing: a complete in vivo evaluation, J. Biomed. Nanotechnol. 17 (5) (2021) 889–900.

[38] E.G. Bajsić, B. Mijović, N.V. Penava, T.H. Grgurić, M. Slouf, E. Zdraveva, The effect of UV irradiation on the electrospun PCL/TiO2 composites fibers, J. Appl. Polym. Sci. 133 (24) (2016).

[39] K. Ohkawa, D. Cha, H. Kim, A. Nishida, H. Yamamoto, Electrospinning of chitosan, Macromol. Rapid Commun. 25 (18) (2004) 1600–1605.

[40] F.M. Ghorbani, B. Kaffashi, P. Shokrollahi, E. Seyedjafari, A. Ardeshirylajimi, PCL/chitosan/Zn-doped nHA electrospun nanocomposite scaffold promotes adipose derived stem cells adhesion and proliferation, Carbohydr. Polym. 118 (2015) 133–142.

[41] M. Tominac Trcin, E. Zdraveva, T. Dolenec, I. Vrgoč Zimić, M. Bujić Mihica, I. Batarilo, I. Dekaris, V. Blažević, I. Slivac, T. Holjevac Grgurić, E.G. Bajsić, K. Markov, I. Čanak, S. Kuzmić, A. Tarbuk, A. Tomljenović, N. Mrkonjić, B. Mijović, Poly(ε-caprolactone) titanium dioxide and cefuroxime antimicrobial scaffolds for cultivation of human Limbal stem cells, Polymers 12 (8) (2020) 1758.

[42] X. Gu, R. Cao, Y. Li, S. Liu, Z. Wang, S. Feng, F. Li, S. Lyu, Three-component antibacterial membrane of poly(butylene carbonate), poly(lactic acid) and chitosan prepared by electrospinning, Mater. Technol. 34 (8) (2019) 463–470.

[43] J. Yin, L. Xu, Batch preparation of electrospun polycaprolactone/chitosan/aloe vera blended nanofiber membranes for novel wound dressing, Int. J. Biol. Macromol. 160 (2020) 352–363.

[44] H. Chen, X. Fan, J. Xia, P. Chen, X. Zhou, J. Huang, J. Yu, P. Gu, Electrospun chitosan-graft-poly (ε-caprolactone)/poly (ε-caprolactone) nanofibrous scaffolds for retinal tissue engineering, Int. J. Nanomedicine 6 (2011) 453–461.

[45] Y. Guo, D. He, S. Xia, X. Xie, X. Gao, Q. Zhang, Preparation of a novel nanocomposite of polyaniline core decorated with Anatase-TiO2 nanoparticles in ionic liquid/water microemulsion, J. Nanomater. 2012 (2012) 202794.

[46] G. Sivalingam, R. Karthik, G. Madras, Kinetics of thermal degradation of poly (ε-caprolactone), J. Anal. Appl. Pyrolysis 70 (2) (2003) 631–647.

[47] K. Fukushima, D. Tabuani, G. Camino, Nanocomposites of PLA and PCL based on montmorillonite and sepiolite, Mater. Sci. Eng. C 29 (4) (2009) 1433–1441.

[48] I. Corazzari, R. Nisticò, F. Turci, M.G. Faga, F. Franzoso, S. Tabasso, G. Magnacca, Advanced physico-chemical characterization of chitosan by means of TGA coupled on-line with FTIR and GCMS: thermal degradation and water adsorption capacity, Polym. Degrad. Stab. 112 (2015) 1–9.

[49] S. Ramasundaram, A. Son, M.G. Seid, S. Shim, S.H. Lee, Y.C. Chung, C. Lee, J. Lee, S.W. Hong, Photocatalytic applications of paper-like poly(vinylidene fluoride)–titanium dioxide hybrids fabricated using a combination of electrospinning and electrospraying, J. Hazard. Mater. 285 (2015) 267–276.

[50] M. Sudhakaran, S. Shabin, N. S, S. Jagadeeshan, Fabrication and characterization of electrospun poly(ε-caprolactone) / TiO2 nanocomposite membranes with synergistic antibacterial property with gentamicin against MRSA, Int. J. Sci. Eng. Res. 6 (2015) 1638–1647.

[51] S. Bonardd, M. Schmidt, M. Saavedra-Torres, A. Leiva, D. Radic, C. Saldías, Thermal and morphological behavior of chitosan/PEO blends containing gold nanoparticles. Experimental and theoretical studies, Carbohydr. Polym. 144 (2016) 315–329.

[52] C.T. Lim, E.P.S. Tan, S.Y. Ng, Effects of crystalline morphology on the tensile properties of electrospun polymer nanofibers, Appl. Phys. Lett. 92 (14) (2008) 141908.

[53] H.-H. Kao, C.-Y. Kuo, D. Tagadur Govindaraju, K.-S. Chen, J.-P. Chen, Polycaprolactone/chitosan composite nanofiber membrane as a preferred scaffold for the culture of mesothelial cells and the repair of damaged mesothelium, Int. J. Mol. Sci. 23 (17) (2022) 9517.

[54] H. Golipour, E. Ezzatzadeh, A. Sadeghianmaryan, Investigation of co-electrospun gelatin: TiO2/polycaprolactone:silk fibroin scaffolds for wound healing applications, J. Appl. Polym. Sci. 139 (27) (2022).

[55] M. Thommes, K. Kaneko, A.V. Neimark, J.P. Olivier, F. Rodriguez-Reinoso, J. Rouquerol, K.S.W. Sing, Physisorption of Gases, With Special Reference to the Evaluation of Surface Area and Pore Size Distribution (IUPAC Technical Report) 87 (9–10), 2015, pp. 1051–1069.

[56] D.F. Ollis, Kinetics of Photocatalyzed Reactions: Five Lessons Learned, Frontiers in Chemistry 6, 2018.

[57] K.P. Gopinath, N.V. Madhav, A. Krishnan, R. Malolan, G. Rangarajan, Present applications of titanium dioxide for the photocatalytic removal of pollutants from water: a review, J. Environ. Manag. 270 (2020) 110906.

[58] C.S. Turchi, D.F. Ollis, Photocatalytic degradation of organic water contaminants: mechanisms involving hydroxyl radical attack, J. Catal. 122 (1) (1990) 178–192.

[59] U.I. Gaya, A.H. Abdullah, Heterogeneous photocatalytic degradation of organic contaminants over titanium dioxide: a review of fundamentals, progress and problems, J Photochem Photobiol C: Photochem Rev 9 (1) (2008) 1–12.

[60] J. Yao, H. Chen, F. Jiang, Z. Jiao, M. Jin, Titanium dioxide and cadmium sulfide co-sensitized graphitic carbon nitride nanosheets composite photocatalysts with superior performance in phenol degradation under visible-light irradiation, J. Colloid Interface Sci. 490 (2017) 154–162.

[61] M.N. Chong, B. Jin, C.W.K. Chow, C. Saint, Recent developments in photocatalytic water treatment technology: a review, Water Res. 44 (10) (2010) 2997–3027.

[62] Y. Ma, J.-n. Yao, Photodegradation of Rhodamine B catalyzed by TiO2 thin films, J. Photochem. Photobiol. A Chem. 116 (2) (1998) 167–170.

[63] C. Guo, J. Xu, Y. He, Y. Zhang, Y. Wang, Photodegradation of rhodamine B and methyl orange over one-dimensional TiO2 catalysts under simulated solar irradiation, Appl. Surf. Sci. 257 (8) (2011) 3798–3803.

[64] C. Chen, W. Ma, J. Zhao, Semiconductor-mediated photodegradation of pollutants under visible-light irradiation, Chem. Soc. Rev. 39 (11) (2010) 4206–4219.

[65] J. Alvarez-Ramirez, R. Femat, M. Meraz, C. Ibarra-Valdez, Some remarks on the Langmuir–Hinshelwood kinetics, J. Math. Chem. 54 (2) (2016) 375–392.

[66] K.V. Kumar, K. Porkodi, F. Rocha, Langmuir–Hinshelwood kinetics – a theoretical study, Catal. Commun. 9 (1) (2008) 82–84.